

Edge states of hydrogen terminated monolayer materials: silicene, germanene and stanene ribbons

A Hattori¹, S Tanaya², K Yada¹, M Araidai^{3,4}, M Sato⁵, Y Hatsugai², K Shiraishi³, Y Tanaka¹

¹ Department of Applied Physics, Nagoya University, Nagoya 464-8603, Japan

² Division of Physics, Faculty of Pure and Applied Sciences, University of Tsukuba, Tsukuba, Ibaraki 305-8571, Japan

³ Institute of Materials and Systems for Sustainability, Nagoya University, Nagoya 464-8603, Japan

⁴ Institute for Advanced Research, Nagoya University, Nagoya 464-8601, Japan

⁵ Yukawa Institute for Theoretical Physics, Kyoto University, Kyoto 606-8502, Japan

E-mail: hattori@rover.nuap.nagoya-u.ac.jp

Abstract.

We investigate the energy dispersion of the edge states in zigzag silicene, germanene and stanene nanoribbons with and without hydrogen termination based on a multi-orbital tight-binding model. Since the low buckled structures are crucial for these materials, both the π and σ orbitals have a strong influence on the edge states, different from the case for graphene nanoribbons. The obtained dispersion of helical edge states is nonlinear, similar to that obtained by first-principles calculations. On the other hand, the dispersion derived from the single-orbital tight-binding model is always linear. Therefore, we find that the non-linearity comes from the multi-orbital effects, and accurate results cannot be obtained by the single-orbital model but can be obtained by the multi-orbital tight-binding model. We show that the multi-orbital model is essential for correctly understanding the dispersion of the edge states in tetragen nanoribbons with a low buckled geometry.

Keywords: edge states, multi-orbital model, low-buckled structure, non-linear dispersion

Submitted to: *J. Phys.: Condens. Matter*

(Some figures may appear in colour only in the online journal)

1. Introduction

Silicene, germanene and stanene are quasi-two dimensional graphene-like materials composed of silicon, germanium and tin atoms, respectively. Graphene has massless Dirac cones at the K and K' points in the Brillouin zone at which the π and π^* bands linearly cross the Fermi level. The electronic properties of silicene, germanene and stanene are akin to those of graphene; however, the Dirac cones become massive due to spin-orbit coupling [1–4]. These three materials prefer to construct sp^3 -like hybridized orbitals rather than sp^2 ones and exhibit low buckled structures, different from that of graphene. Owing to this low buckled structure, these three materials have ambipolar properties and the magnitude of the energy gap is tunable by an electric field [5–7]. For these materials, quantum spin Hall (QSH) effects are predicted and can be observed at room temperature in stanene [8, 9]. Silicene sheets have been synthesized on Ag [10–15], ZrB₂ [16] and Ir [17] substrates under ultra-high pressure vacuum [18], and it has been reported that germanene has been synthesized on substrates of Au and Pt [19, 20] and stanene has been synthesized on Bi₂Te₃ [21].

Several studies of tetragen nanoribbons have been reported. For graphene nanoribbons (GrNRs), a flat band zero energy edge state is generated from the K point to the zone boundary in a zigzag edge and from the Γ to K points in a Klein edge [22–27]. In actual experiments, the hydrogen termination effect is important as it has a strong influence on the edge states of GrNRs [28–30]. Zigzag graphene nanoribbons (ZGrNRs) with mono-hydrogen termination at the edge sites reproduce the zigzag edge states [31–34]. On the other hand, ZGrNRs with di-hydrogen termination at the edge sites reproduce the Klein edge state [35, 36].

The electronic properties of the edge states of silicene, germanene and stanene nanoribbons (SiNRs, GeNRs, SnNRs) with and without hydrogen termination have also been studied using a single-orbital tight-binding model [4, 7] and first-principles calculations [37–41] by many groups. Although the single-orbital model can reproduce the bulk energy dispersion [42], it has not yet been clarified whether the single-orbital model can really express the various types of edge states with hydrogen termination [4]. On the other hand, it has been reported based on first-principles calculations that the single-orbital model cannot correctly express the dispersion of hydrogen terminated edge states of zigzag germanene nanoribbons (ZGeNRs) [43]. Although the single-orbital tight-binding model is too simple to reproduce the correct edge state, it is not clear whether a multi-orbital model can correctly express the hydrogen terminated edge states.

In this paper, we construct multi-orbital tight-binding models for zigzag silicene nanoribbons (ZSiNRs), ZGeNRs and zigzag stanene nanoribbons (ZSnNRs). The parameters are extracted from the density-functional theory (DFT) results for simple tetragen molecules. We show that the energy dispersion derived from the DFT calculations can be successfully reproduced by our multi-orbital tight-binding model with the parameters. In the case of mono-hydrogen termination, zigzag-like edge

states are realized, while in the di-hydrogen termination case, Klein-like edge states are realized. We obtain the nonlinear dispersion of the edge states, which is different from that based on a single-orbital model and is consistent with the results of first-principles calculations [43]. Based on these results, we find that the origin of this nonlinear dispersion is the sp^3 -like hybridized orbitals. This shows that the multi-orbital tight-binding model is useful for studying the electronic properties of nanoribbons including the edge states.

The organization of this paper is as follows. In Section 2, we explain the model and formulation as well as the structure of the nanoribbons, the multi-orbital tight-binding model and the material parameters. We also explain how the coupling constants for Si-H, Ge-H, Sn-H bonds and the on-site energies of each orbital are determined. In Section 3, we show the results of our numerical calculations, including the energy spectra of zigzag nanoribbons (ZNRs) with and without hydrogen termination. In Section 4, we summarize our results.

2. Models and Formulations

2.1. Atomic structure of nanoribbons

SiNRs, GeNRs and SnNRs have low buckled honeycomb structures, as shown in Figure 1. The buckling angle θ is defined as shown in Figure 1(a). The vectors from the B site to the three neighboring A sites (\vec{d}_1 , \vec{d}_2 and \vec{d}_3) are given by

$$\vec{d}_1 = a \sin \theta (1, 0, \cot \theta), \quad (1)$$

$$\vec{d}_2 = a \sin \theta \left(-\frac{1}{2}, \frac{\sqrt{3}}{2}, \cot \theta\right), \quad (2)$$

$$\vec{d}_3 = a \sin \theta \left(-\frac{1}{2}, -\frac{\sqrt{3}}{2}, \cot \theta\right), \quad (3)$$

with a lattice constant a . Here we consider nanoribbon systems which have periodic boundaries along the y -axis, as shown in Figures 1(b) and (c). The width of the nanoribbons is denoted by $2w$. Figures 1(b) and (c) show two kinds of hydrogen termination (mono-hydrogen and di-hydrogen termination). Considering the sp^3 nature of tetragens, we choose the position vectors of the hydrogen site from the tetragen site at the rightmost edge to be

$$\vec{d}_{H_1} = a_H (\sin \theta, 0, \cos \theta), \quad (4)$$

$$\vec{d}_{H_2} = a_H (0, 0, 1), \quad (5)$$

where a_H is the distance between a hydrogen and a tetragen. The azimuthal angle θ is chosen to be the same as the buckling angle. The position vectors for the left edge are opposite to those of the rightmost edge, i.e., $\vec{d}_{H_3} = -\vec{d}_{H_1}$ and $\vec{d}_{H_4} = -\vec{d}_{H_2}$. In this paper, we consider three kinds of hydrogen termination: mono-hydrogen termination at the outermost edges (1H/1H), di-hydrogen termination at the outermost edges (2H/2H) and raw edges without hydrogen termination (0H/0H).

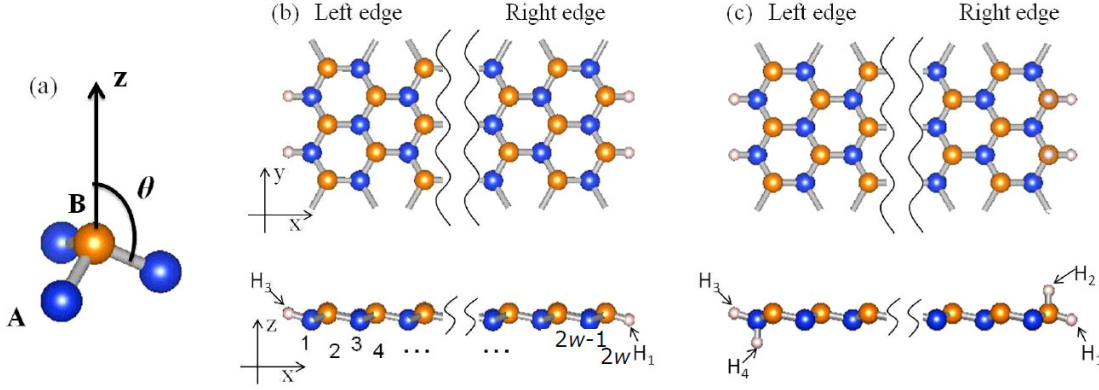


Figure 1. (a) Illustration of θ , defined as being the angle between the direction from the B site (orange) to the A site (blue) and the z -axis normal to the plane. (b), (c) Lattice geometry of ZNRs with hydrogen termination at both edge sites: (b) 1H/1H and (c) 2H/2H. The upper and lower panels show the top and side views.

2.2. Multi-orbital tight-binding model

The multi-orbital tight-binding model used in this paper consists of four outer-shell orbitals (s , p_x , p_y and p_z orbitals) of tetragens and a $1s$ -orbital of hydrogen. The Hamiltonian \mathcal{H} is given by

$$\mathcal{H} = \mathcal{H}_0 + \mathcal{H}_{\text{so}} + \mathcal{H}_{\text{H}}. \quad (6)$$

The first term \mathcal{H}_0 denotes the on-site energy of the tetragens and nearest neighbor hopping between them:

$$\begin{aligned} \mathcal{H}_0 = & \sum_{\langle i,j \rangle} \sum_{\alpha,\beta} \sum_{\tau} (t_{i,j}^{\alpha\beta} c_{i\alpha\tau}^\dagger c_{j\beta\tau} + \text{h.c.}) \\ & + \sum_i \sum_{\alpha} \sum_{\tau} \epsilon_{\alpha} c_{i\alpha\tau}^\dagger c_{i\alpha\tau}, \end{aligned} \quad (7)$$

where $c_{i\alpha\tau}^\dagger$ and $c_{i\alpha\tau}$ are the creation and annihilation operators for an electron with an atomic orbital α and a spin τ at site i . ϵ_{α} denotes the site energy for orbital α . The first term in equation (7) corresponds to the hybridization between tetragens and the second term represents the on-site energy at the tetragen sites. $\langle i,j \rangle$ runs over all the nearest neighbor hopping sites. The hopping integral $t_{i,j}^{\alpha\beta}$ is determined by the Slater-Koster parameters $V_{ss\sigma}$, $V_{sp\sigma}$, $V_{pp\sigma}$ and $V_{pp\pi}$, as shown in Table 1. The second term \mathcal{H}_{so} expresses the spin-orbit interaction

$$\mathcal{H}_{\text{so}} = \frac{\xi_0}{2} \sum_i \sum_{\bar{\alpha}\bar{\beta}\bar{\gamma}} \sum_{\tau,\tau'} \epsilon_{\bar{\alpha}\bar{\beta}\bar{\gamma}} c_{i\bar{\alpha}\tau}^\dagger (-i\hat{\sigma}_{\bar{\gamma}}) c_{i\bar{\beta}\tau'} + \text{h.c.}, \quad (8)$$

where ξ_0 is the strength of the spin-orbit coupling, $\bar{\alpha} = x, y, z$, $\bar{\beta} = x, y, z$ and $\bar{\gamma} = x, y, z$ are indices of the $p_{\bar{\alpha}}$, $p_{\bar{\beta}}$ and $p_{\bar{\gamma}}$ orbitals. $\epsilon_{\bar{\alpha}\bar{\beta}\bar{\gamma}}$ is an antisymmetric tensor and $\hat{\sigma}_{\bar{\gamma}}$ is the Pauli matrix acting on the spin space. The third term of \mathcal{H}_{H} describes the hydrogen

Table 1. Slater–Koster interatomic matrix elements [44]. The matrix elements for nearest neighbor hopping between s and p orbitals are determined by the direction cosines l_{ij} , m_{ij} and n_{ij} which are the x , y and z components measured from site i to site j .

t_{ij}^{ss}	$V_{ss\sigma}$
t_{ij}^{sx}	$l_{ij}V_{sp\sigma}$
t_{ij}^{sy}	$-l_{ij}V_{sp\sigma}$
t_{ij}^{sx}	$l_{ij}^2V_{pp\sigma} + (1 - l_{ij}^2)V_{pp\pi}$
t_{ij}^{xy}	$l_{ij}m_{ij}(V_{pp\sigma} - V_{pp\pi})$
t_{ij}^{xz}	$m_{ij}n_{ij}(V_{pp\sigma} - V_{pp\pi})$

Table 2. Numerical values of parameters in multi-orbital tight-binding models. The lattice constants a and the buckling angles θ are given by Liu *et al.* [42]. The hopping parameters between tetragens are chosen according to Ref. [45] for C-C bonds, Ref. [46] for Si-Si and Ge-Ge bonds and Ref. [47] for Sn-Sn bonds. The strength of the spin-orbit coupling ξ_0 for graphene, silicene (germanene) and stanene are obtained based on Yao *et al.* [48], Liu *et al.* [5] and Chadi [49].

System	$a(\text{\AA})$	$\theta(\text{deg})$	$V_{ss\sigma}(\text{eV})$	$V_{sp\sigma}(\text{eV})$	$V_{pp\sigma}(\text{eV})$	$V_{pp\pi}(\text{eV})$	$\xi_0(\text{eV})$
Graphene	2.46	90	-6.769	5.580	5.037	-3.033	9×10^{-3}
Silicene	3.86	101.7	-1.93	2.54	4.47	-1.12	34×10^{-3}
Germanene	4.02	106.5	-1.79	2.36	4.15	-1.04	0.196
Stanene	4.70	107.1	-2.6245	2.6504	1.4926	-0.7877	0.8

termination:

$$\begin{aligned}
\mathcal{H}_H = & \sum_{\langle i,j \rangle} \sum_{\alpha} \sum_{\tau} (t_{ij}^{s\alpha} d_{is\tau}^{\dagger} c_{j\alpha\tau} + \text{h.c.}) \\
& + \sum_i \sum_{\tau} \epsilon_H d_{is\tau}^{\dagger} d_{is\tau},
\end{aligned} \tag{9}$$

where $d_{is\tau}^{\dagger}$ and $d_{is\tau}$ are the creation and annihilation operators for an electron at hydrogen site i . The first term in equation (9) corresponds to the hybridization of hydrogen and tetragen, and the second term is the on-site energy at the hydrogen sites. ϵ_H denotes the site energy for an electron at a hydrogen atom. The hopping parameters for the tetragens' bonds, i.e., the values of $V_{ss\sigma}$, $V_{sp\sigma}$, $V_{pp\sigma}$ and $V_{pp\pi}$, are given in Table 2. The hopping parameters between tetragens and hydrogens are given in Table 3, which will be explained in Section 2.4.

Table 3. Parameters of C-H, Si-H, Ge-H and Sn-H bonds and the difference in on-site energies (eV) in the multi-orbital tight-binding model.

System	$V_{ss\sigma}$	$V_{sp\sigma}$	ϵ_s	$\epsilon_s - \epsilon_H$	$\epsilon_s - \epsilon_p$
Graphene	-10.457 [50]	13.744 [50]	-17.52 [50]	-3.87 [50, 51]	-8.55 [51]
Silicene	-3.18	3.32	-7.90	-1.97	-5.44
Germanene	-3.29	2.66	-7.90	-1.00	-6.74
Stanene	-2.75	3.27	-9.00	-4.38	-5.61

Table 4. Material parameters in effective model [4, 42].

System	t (eV)	λ_{so} (meV)	λ_R (meV)	l (Å)
Graphene	2.8	10^{-3}	0	0
Silicene	1.07	3.97	0.7	0.23
Germanene	0.991	46.3	10.7	0.33
Stanene	0.760	64.4	9.5	0.40

2.3. Low-energy effective Hamiltonian

In this subsection, we explain the single-orbital model which effectively expresses the low-energy dispersion around the K and K' points [42]. The Hamiltonian \mathcal{H}_{eff} in the single-orbital model is given by

$$\begin{aligned}
\mathcal{H}_{\text{eff}} = & -t \sum_{\langle i,j \rangle} \sum_{\tau} c_{i\tau}^{\dagger} c_{j\tau} + i \frac{\lambda_{so}}{3\sqrt{3}} \sum_{\langle\langle i,j \rangle\rangle} \sum_{\tau\tau'} v_{ij} c_{i\tau}^{\dagger} \sigma_{\tau\tau'}^z c_{j\tau'} \\
& - i \frac{2}{3} \lambda_R \sum_{\langle\langle i,j \rangle\rangle} \sum_{\tau\tau'} \mu_i c_{i\tau}^{\dagger} (\sigma \times \hat{d}_{ij})_{\tau\tau'}^z c_{j\tau'},
\end{aligned} \tag{10}$$

where $c_{i\tau}^{\dagger}$ and $c_{i\tau}$ are creation and annihilation operators with spin τ at site i . The first term represents nearest neighbor hopping. The second and third terms are the effective spin-orbit coupling and the intrinsic Rashba spin-orbit coupling, respectively. $\langle\langle i, j \rangle\rangle$ runs over all the next nearest neighbor sites. As shown by Kane and Mele [52], $v_{i,j} = +1$ or -1 if the direction from j to i site is anticlockwise or clockwise in the hexagon. $\sigma_{\tau\tau'}^z$ denotes an element of the Pauli matrix acting on the spin space. $\mu_i = 1$ and -1 for the A or B site and $\hat{d}_{i,j}$ is given by $\hat{d}_{i,j} = \vec{d}_{i,j}/|\vec{d}_{i,j}|$, where $\vec{d}_{i,j}$ is a vector from site i to the second nearest neighbor site j . The material parameters for a single-orbital Hamiltonian are shown in Table 4 [4, 42]. Here, t and λ_{so} are based on a paper by Liu *et al.* [42].

2.4. Determination of parameters for Si-H, Ge-H and Sn-H bonds and on-site energies

In this subsection, we explain how to determine the values of the binding energies for Si-H, Ge-H and Sn-H bonds and the on-site energy of each orbital in Table 3. For this purpose, we need the interatomic elements for coupled silicon, germanium and tin and hydrogen atoms. We determine these elements from molecules that have Si-H, Ge-H and Sn-H bonds. In this paper, we use the simple molecules silane (SiH_4), germane (GeH_4) and stannane (SnH_4). For these molecules, we assume a multi-orbital Hamiltonian \mathcal{H}_{mol} with nearest neighbor hopping. In the case of silane, the relevant orbitals are $\{3s, 3p_x, 3p_y, 3p_z, 1s, 1s, 1s, 1s\}$. \mathcal{H}_{mol} is given by

$$\begin{aligned} \mathcal{H}_{\text{mol}} = & \sum_{\langle i,j \rangle} \sum_{k=0}^3 \sum_{\alpha} \sum_{\tau} (t_{ij}^{s\alpha} d_{i\sigma\tau}^{(k)\dagger} c_{j\alpha\tau} + \text{h.c.}) \\ & + \sum_i \sum_{k=0}^3 \sum_{\alpha} \sum_{\tau} (\epsilon_H d_{i\sigma\tau}^{(k)\dagger} d_{i\sigma\tau}^{(k)} + \epsilon_{\alpha} c_{i\alpha\tau}^{\dagger} c_{i\alpha\tau}). \end{aligned} \quad (11)$$

From this 8×8 Hamiltonian, we can analytically obtain eight eigenvalues which depend on the interatomic elements ($V_{ss\sigma}$, $V_{sp\sigma}$) and on-site energies (ϵ_s , ϵ_p , ϵ_H), as shown in Appendix A. The four obtained energy eigenvalues have a single degeneracy and triple degeneracies at the HOMO and LUMO levels, respectively. They are given by

$$\lambda_1^{\pm} = \frac{\epsilon_H + \epsilon_s \pm \sqrt{(\epsilon_H - \epsilon_s)^2 + 16V_{ss\sigma}^2}}{2}, \quad (12)$$

$$\lambda_3^{\pm} = \frac{\epsilon_H + \epsilon_p \pm \sqrt{(\epsilon_H - \epsilon_p)^2 + 16V^2}}{2}, \quad (13)$$

with $V = V_{sp\sigma}/\sqrt{3}$, where λ_1^{\pm} has a single degeneracy and λ_3^{\pm} have triple degeneracies. The values of λ_1^{\pm} and λ_3^{\pm} are determined by first-principles calculations, as shown in Table 5 [53]. Then, by using equations (12) and (13), we determine five parameters while the number of equations is four. Thus, we first obtain a value of ϵ_s as a parameter. Then the other four parameters are given by the following expressions:

$$\epsilon_p = \epsilon_s - (\lambda_1^+ + \lambda_1^-) + (\lambda_3^+ + \lambda_3^-), \quad (14)$$

$$\epsilon_H = -\epsilon_s + (\lambda_1^+ + \lambda_1^-), \quad (15)$$

$$V_{ss\sigma} = \frac{\sqrt{(\lambda_1^+ - \lambda_1^-)^2 - (\epsilon_H - \epsilon_s)^2}}{4}, \quad (16)$$

$$V = \frac{\sqrt{(\lambda_3^+ - \lambda_3^-)^2 - (\epsilon_H - \epsilon_p)^2}}{4}. \quad (17)$$

equations (16) and (17) require $(\lambda_1^+ - \lambda_1^-)^2 - (\epsilon_H - \epsilon_s)^2 > 0$ and $(\lambda_3^+ - \lambda_3^-)^2 - (\epsilon_H - \epsilon_p)^2 > 0$, giving the following constraint

$$\begin{cases} \lambda_1^- < \epsilon_s < \lambda_1^+ \\ \lambda_1^+ + \lambda_1^- - \lambda_3^+ < \epsilon_s < \lambda_1^+ + \lambda_1^- - \lambda_3^-. \end{cases} \quad (18)$$

Table 5. Energy levels (eV) of SiH₄, GeH₄ and SnH₄ obtained by first-principles calculations [53].

System	λ_3^+	λ_1^+	λ_3^-	λ_1^-
Silane	0.00880	-0.475	-8.40	-13.4
Germane	0.169	-0.790	-8.23	-14.0
Stannane	-0.181	-0.882	-7.82	-12.7

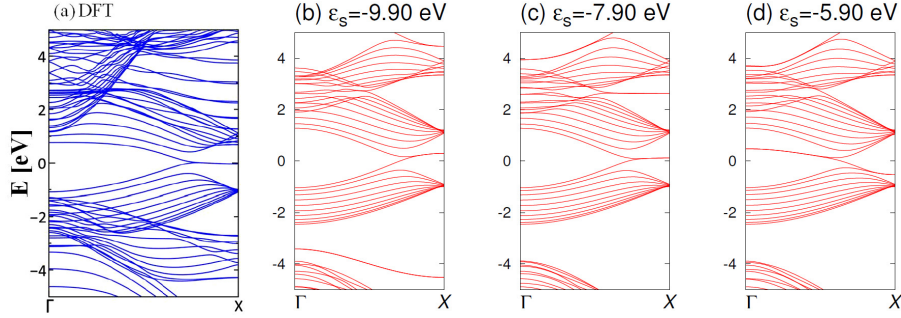


Figure 2. Energy spectra for 1H/1H ZSiNRs ($w = 10$). (a) First-principles calculation. [53] (b), (c), (d) Calculation using multi-orbital tight-binding model: (b) $\epsilon_s = -9.90$ eV, (c) $\epsilon_s = -7.90$ eV, (d) $\epsilon_s = -5.90$ eV.

Using equation (18), we can determine the values of ϵ_s to be for Si: $-13.4 < \epsilon_s < -5.43$, Ge: $-14.0 < \epsilon_s < -6.57$ and Sn: $-12.7 < \epsilon_s < -5.79$. Substituting these material parameters into the Hamiltonian for the ZNRs \mathcal{H} given in equation (6), we can calculate the energy spectra for ZNRs with hydrogen termination at the outermost edge sites and compare with those obtained by first-principles calculations for $w = 10$ [53]. We compare the energy spectra obtained by the multi-orbital model with 1H/1H and 2H/2H ZNRs and those by first-principles calculations, and optimize the value of ϵ_s for ZSiNRs, ZGeNRs and ZSnNRs. Figure 2 shows energy spectra for 1H/1H ZSiNRs using (a) first-principles calculations and (b)–(d) the multi-orbital tight-binding model. We have chosen $\epsilon_s = -7.90$ eV since we can qualitatively reproduce the energy spectra obtained by first-principles calculations. We can also reproduce the energy spectra for 2H/2H ZSiNRs obtained by first-principles calculations. Similarly, we have chosen values of ϵ_s for ZGeNRs and ZSnNRs as summarized in Table 3.

3. Results

3.1. ZNRs without hydrogen termination

In this subsection, we calculate the energy spectra for ZNRs without hydrogen termination for $w = 100$. By comparing the results obtained by the single-orbital model with those by the multi-orbital model, we demonstrate the benefit of using the

Table 6. Numerically obtained parameters for Si-H (eV).

ϵ_s	-9.90	-7.90	-5.90
$\epsilon_s - \epsilon_p$	-5.44	-5.44	-5.44
$\epsilon_s - \epsilon_H$	-5.97	1.62	2.03
$V_{ss\sigma}$	-2.85	-3.18	-3.18
$V_{sp\sigma}$	3.64	3.32	1.67

multi-orbital model to study the energy spectra for ZNRs having low buckled geometries.

First, we show the energy spectra for ZGrNRs based on the (a) single-orbital and (b) multi-orbital models in Figure 3. In the figure, both the single-orbital model and the multi-orbital model exhibit a flat band in the momentum space $2\pi/3 \leq |k_y| \leq \pi$ at the Fermi level. The energy spectrum for the single-orbital model qualitatively reproduces that for the multi-orbital model except for the in-gap states at $-0.4\pi \leq k_y \leq 0.4\pi$, shown in Figure 3(b). Figures 3(c) and (d) show the orbital decomposed probability density $|\Psi(\alpha)|^2$ ($\alpha = s, p_x, p_y, p_z$) of the flat band and in-gap states, respectively. $|\Psi(p_z)|^2$ of the flat band at $k_y = \pi$ is localized only at the outermost edge sites. This feature agrees with that for the single-orbital model as shown in Figure 3(c). Therefore, the flat band in Figures 3(a) and (b) corresponds to the zigzag edge states. On the other hand, the in-gap states at $-0.4\pi \leq k_y \leq 0.4\pi$ in the multi-orbital model mainly consist of the p_x orbital around the edge sites of ZGrNRs, and $|\Psi(p_x)|^2$ oscillates with damping from the outermost edge sites to the inner sites as shown in Figure 3(d). Since the σ orbitals composed of $2s$, $2p_x$ and $2p_y$ components are orthogonal to the $2p_z$ (π) orbital in ZGrNRs, the flat band originates only from the π -bonds. Then, without considering the multi-orbital effect, non-zero edge states do not appear. The non-zero edge state is a dangling bond on a carbon atom at the edge site of ZGrNRs. The carbon $2s$, $2p_x$ and $2p_y$ orbitals are essential for describing both the dangling bonds and the orbital hybridizations between carbon and hydrogen, as shown in the next subsection.

Next, we show the energy spectrum for ZSiNRs without hydrogen termination. As seen from Figure 4, the bulk energy spectra for the single-orbital model (Figure 4(a)) and the multi-orbital model (Figure 4(b)) are similar. However while there exists a nearly flat band in the single-orbital model similar to the graphene case (Figures 3(a) and (b)), there is no such band in the multi-orbital model, as shown in Figure 4(b). In the multi-orbital model, instead of a flat band, in-gap states with dispersion appear for $2\pi/3 \leq |k_y| \leq \pi$ with positive energy and for $-2\pi/3 \leq k_y \leq 2\pi/3$ with negative energy. We find that the in-gap states in Figure 4(b) are completely different from the flat band in Figure 4(a). In addition, $|\Psi(\alpha)|^2$ for the in-gap states at $k_y = \pi$ in Figure 4(c) and $k_y = 0$ in Figure 4(d) have different orbital components. The in-gap states at $k_y = \pi$ mainly consist of p_z orbitals localized at the outermost edge sites. On the other hand, the in-gap states at $k_y = 0$ mainly consist of p_x orbitals localized at the outermost edge

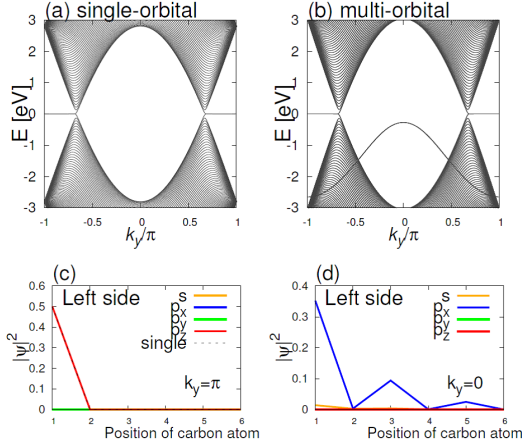


Figure 3. Energy spectra for ZGrNRs ($w = 100$) calculated by (a) the single-orbital model and (b) the multi-orbital model (0H/0H). Orbital decomposed probability density of edge states (c) $k_y = \pi$ and (d) $k_y = 0$ in 0H/0H ZGrNRs.

sites and p_z orbitals localized at the first neighbor to the outermost edge sites. This feature is different from the in-gap states for ZGrNRs without hydrogen termination in Figure 3(d).

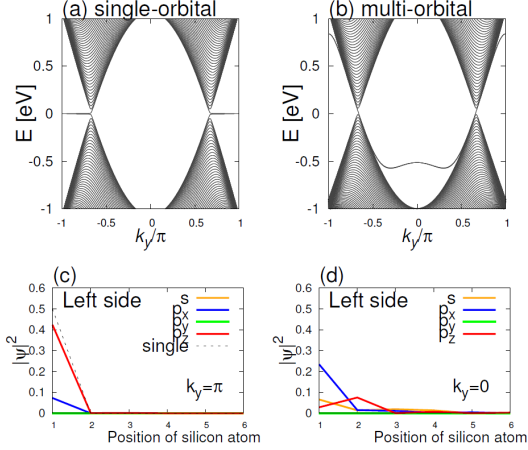


Figure 4. Energy spectra for ZSiNRs ($w = 100$) calculated by (a) the single-orbital model and (b) the multi-orbital model (0H/0H). Orbital decomposed probability density of edge states at (c) $k_y = \pi$, (d) $k_y = 0$ in 0H/0H ZSiNRs.

Next, we show the energy spectra for ZGeNRs in Figure 5. Comparing the results of the single-orbital model (Figure 5(a)) and the multi-orbital model (Figure 5(b)), the dispersion of the in-gap states is completely different while the bulk energy spectra are similar, as in the case of ZSiNRs. To be specific, in the case of the single-orbital model, the upper and lower branches of the resulting in-gap states show a linear dispersion and cross each other at $k_y = \pm\pi$ (Figure 5(a)) where time-reversal invariance is satisfied. A bulk energy gap opens at $k_y = \pm 2\pi/3$ due to the spin-orbit coupling. This in-gap state can be regarded as a typical helical edge state realized in a QSH insulator.

However, the qualitative features of the in-gap state in the multi-orbital model are different from that for the single-orbital model. As shown in Figure 5(b), the in-gap states for $-2\pi/3 \leq k_y \leq 2\pi/3$ connect between the conduction and valence bands and can be regarded as helical edge states. Although the present in-gap state is located around the Fermi level $E = 0$, it is not symmetric around $E = 0$, in contrast to the case for the single-orbital model. Also, the line shapes and positions of the in-gap states for ZGeNRs are different from those for ZSiNRs. We find from Figure 5(c) that $|\Psi(\alpha)|^2$ for the in-gap states at $k_y = 0$ mainly consists of p_x orbitals at the outermost edge sites and p_z orbitals at the first neighbor to the outermost edge sites, as shown in Figure 5(c).

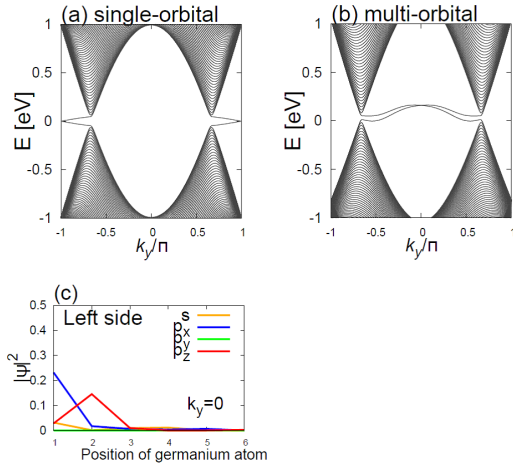


Figure 5. Energy spectra for ZGeNRs ($w = 100$) calculated by (a) the single-orbital model and (b) the multi-orbital model (0H/0H). (c) Orbital decomposed probability density of edge states at $k_y = 0$ in 0H/0H ZGeNRs.

Finally, we focus on the stanene case. Comparing the results of the single-orbital model (Figure 6(a)) and the multi-orbital model (Figure 6(b)), we find that the dispersions of the in-gap states are completely different while the bulk energy spectra are similar except for the extra bands originating from the σ -orbitals around the Γ point ($k_y = 0$). In the case of the single-orbital model, similar to the ZGeNRs case, the in-gap state appears as the edge state of ZSnNRs, as shown in Figure 6(a). The in-gap states with linear dispersion appear around the zone boundary. The bulk energy gap opens at $\pm 2\pi/3$ due to the spin-orbit interaction. On the other hand, the calculated energy dispersion based on the multi-orbital model is very different from that based on the single-orbital model, as shown in Figure 6(b). Two kinds of in-gap states with nonlinear dispersion appear at $2\pi/3 \leq |k_y| \leq \pi$ and $-2\pi/3 \leq k_y \leq 2\pi/3$, and the upper and lower branches cross at $k_y = \pm\pi$ and $k_y = 0$. These in-gap states are expected to be helical edge states and the dispersion of these in-gap states is distinct from that in the single-orbital model. On the other hand, we cannot easily compare our obtained energy dispersion (Figure 6(b)) and first-principles calculations [54] where the spin-orbit coupling is not taken into account. We also note that the bulk energy spectrum with continuum energy levels is generated around $E = 0$ at Γ point, as shown in Figure 6(b).

This energy spectrum is unique to ZSnNRs. It is relevant that the value of $V_{pp\sigma}$ for stanene is smaller than that for other materials. As shown in Figure 6(c), $|\Psi(\alpha)|^2$ for in-gap states at $k_y = \pi$ mainly consists of p_z orbitals at the outermost edge sites and p_y orbitals at the first neighbor to the edge sites. On the other hand, $|\Psi(\alpha)|^2$ for the in-gap states at $k_y = 0$ mainly consists of p_x orbitals localized at the edge sites and p_y orbitals at the inner sites adjacent to this edge sites, as shown in Figure 6(d). Only in the case of ZSnNRs do the p_x and p_y orbital components of the in-gap state penetrate into the inner sites. This is because the energy dispersion for the in-gap states at $k_y = 0$ has a clear slope while those for ZSiNRs and ZGeNRs are almost flat.

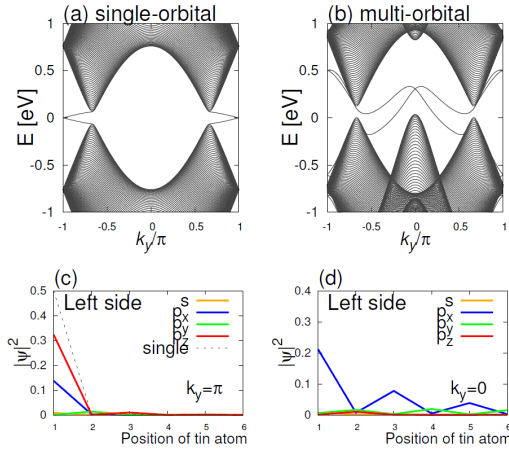


Figure 6. Energy spectra for ZSnNRs ($w = 100$) calculated by (a) the single-orbital model and (b) the multi-orbital model (0H/0H). Orbital decomposed probability density of the edge states at (c) $k_y = \pi$, (d) $k_y = 0$ in 0H/0H ZSnNRs.

In summary, we have calculated energy spectra for ZNRs without hydrogen termination using the multi-orbital model and compared them with those generated by the single-orbital model. In the case of ZGrNRs, it is possible to describe a zigzag edge state by the single-orbital model since the Hamiltonian of GrNRs in the multi-orbital model can be decomposed into two submatrices of σ and π orbitals. On the other hand, the dispersion of the in-gap states for ZSiNRs, ZGeNRs and ZSnNRs with low buckled structures cannot be described by the single-orbital model even though it can express the bulk energy spectra. The multi-orbital Hamiltonians for ZSiNRs, ZGeNRs and ZSnNRs cannot be block diagonalized due to sp^3 -like hybridization. Therefore, the multi-orbital effects are needed to describe the edge states of low buckled material nanoribbons. Thus, we use the multi-orbital model in the following subsections.

3.2. Hydrogen termination effects to ZNRs

In this subsection, we calculate the energy spectra for ZSiNRs, ZGeNRs and ZSnNRs with two types of hydrogen termination, the 1H/1H and 2H/2H cases, with a ribbon width $w = 100$. For ZGrNRs, in an actual experimental situation the dangling bond

states are terminated by a hydrogen atom and the non-zero edge states in Figure 3(b) disappear.

First, the energy spectra for 1H/1H ZNRs are shown in Figures 7(a)–(c). The in-gap states exist at $2\pi/3 \leq |k_y| \leq \pi$ for all materials and they are helical edge states. With an increase in atomic number, the magnitude of the bulk energy gap at $k_y = \pm 2\pi/3$ increases. It becomes the most prominent for ZSnNRs in Figure 7(c), due to the spin–orbit interaction. In addition, the magnitude of the spin splitting of the edge states also increases with the opening of the bulk energy gap. In the case of 1H/1H ZGeNRs (Figure 7(b)), a similar energy dispersion of the edge states is obtained by first-principles calculations [43]. Especially, Figures 7(g) and (h) are qualitatively the same as those determined by first-principles calculations. In addition, the energy dispersion for edge states is non-linear in contrast to the single-orbital model [7]. For 1H/1H ZSiNRs and ZSnNRs, first-principles calculations have been performed without spin–orbit coupling [54–56]. Since the spin–orbit interaction for a silicon atom is weak, the obtained energy dispersion for ZSiNRs (Figure 7(a)) is close to that determined by first-principles calculations [55, 56]. On the other hand, since the spin–orbit interaction for a tin atom is strong, we cannot easily compare the energy dispersion for 1H/1H ZSnNRs using the multi-orbital model (Figure 7(c)) and that by first-principles calculations [54]. $|\Psi(\alpha)|^2$ for the edge states at $k_y = \pm\pi$ is shown in Figures 7(d)–(f). $|\Psi(\alpha)|^2$ mainly consists of p_z orbitals localized at the outermost edge in all cases. The contributions of the s and p_y orbitals are also enhanced near the outermost edge sites. The major contribution from the p_z orbital is a common feature shown in the zigzag edge states in 1H/1H ZGrNRs. Therefore, we can qualitatively regard the mono-hydrogen terminated edge states for ZNRs as zigzag-like edge states.

Next, the energy spectra for 2H/2H ZNRs are shown in Figures 8(a)–(c). The edge states appear at $-2\pi/3 \leq k_y \leq 2\pi/3$, in contrast to the case for 1H/1H ZNRs. With an increase in the spin–orbit coupling, the magnitude of the splitting of the edge states becomes prominent, as in the case of 1H/1H ZNRs. The energy dispersion for the edge states of 2H/2H ZSiNRs is almost two-fold degenerate, similar to 1H/1H ZSiNRs as shown in (a). The location of the edge states is consistent with 2H/2H ZSiNRs in nonmagnetic states by first-principles calculations [56]. With increasing strength of the spin–orbit coupling, we can see spin-split edge states as helical edge states in (b) 2H/2H ZGeNRs and (c) 2H/2H ZSnNRs. We note that an edge mode with a crossing point at $k_y = 0$ is generated.

$|\Psi(\alpha)|^2$ at $k_y = 0$ is plotted for (d) ZSiNRs, (e) ZGeNRs and (f) ZSnNRs in Figure 8. The edge states mainly consist of p_z orbitals localized at the first neighbor to the outermost edge sites. These results are essentially the same as the Klein edge state realized in 2H/2H ZGrNRs.

To summarize this subsection, p_z orbitals make the main contributions to the edge states for ZNRs with various types of hydrogen termination. The obtained edge states do not have completely flat bands similar to those for ZGrNRs due to the orbital hybridization. Moreover, the degree of splitting of the helical edge states becomes

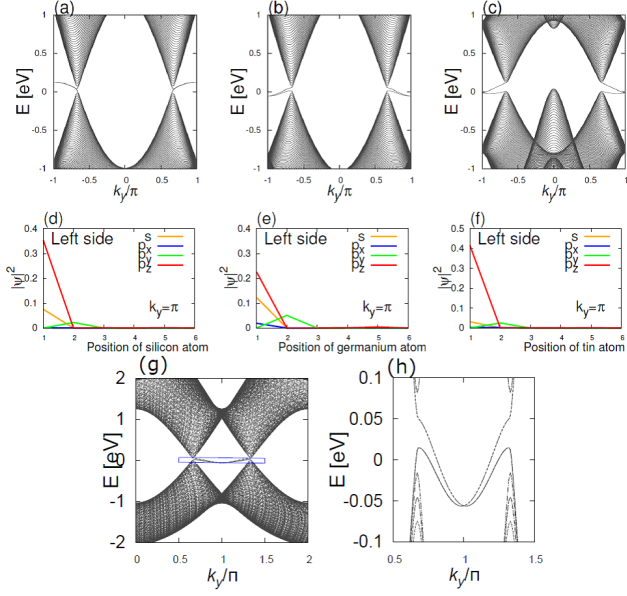


Figure 7. Energy spectra for 1H/1H (a) ZSiNRs, (b) ZGeNRs and (c) ZSnNRs ($w = 100$). Orbital decomposed probability density of edge states at $k_y = \pi$ in (d) 1H/1H ZSiNRs, (e) ZGeNRs and (f) ZSnNRs. (g) Energy dispersion for edge states of 1H/1H ZGeNRs ($w = 100$) plotted at $0 \leq k_y \leq 2\pi$. (h) Enlarged figure of blue frame in (g).

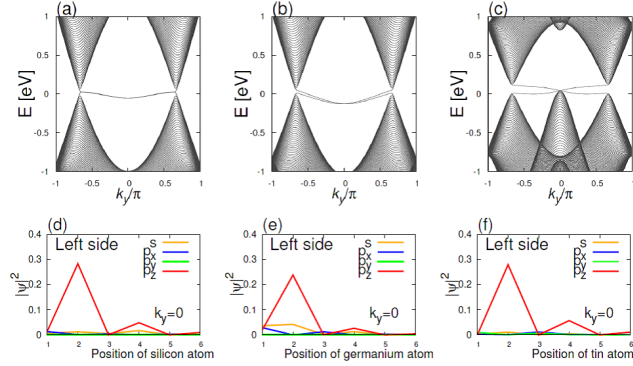


Figure 8. Energy spectra for 2H/2H (a) ZSiNRs, (b) ZGeNRs and (c) ZSnNRs ($w = 100$). Orbital decomposed probability density of edge states at $k_y = 0$ in 2H/2H (d) ZSiNRs, (e) ZGeNRs and (f) ZSnNRs.

stronger with increasing spin-orbit coupling. However, the energy dispersion for the edge states is non-linear due to multi-orbital effects. Our results show that stanene can be regarded as a good example of a QSH system, since the bulk energy gap is sufficiently large to be observed experimentally.

4. Summary and Conclusion

In this paper, we have developed a multi-orbital tight-binding model to study the edge states of zigzag silicene, germanene and stanene nanoribbons. In this study, the

parameters are extracted from the DFT results for simple tetragen molecules. We have shown that the energy dispersion by the DFT calculations can be successfully reproduced by our multi-orbital tight-binding model using these parameters. The obtained dispersion of the edge states is non-linear, similar to the DFT results. On the other hand, the dispersion obtained using the single-orbital tight-binding model is always linear due to the chiral symmetry. Therefore, we find that the non-linearity comes from the multi-orbital effects, and the results cannot be obtained using the single-orbital model but can be obtained using the multi-orbital tight-binding model. This multi-orbital tight-binding model can be readily applied to complicated and much larger systems.

Acknowledgments

The authors would like to thank Mr. Hiroki Shirakawa for his contributions. This work was supported by a Grant-in Aid for Scientific Research on Innovative Areas "Topological Material Science" (Grant No. JP15H05855 and No. JP15H05853), a Grant-in-Aid for Challenging Exploratory Research (Grant No. JP15K13498), the Core Research for Evolutional Science and Technology (CREST) of the Japan Science and Technology Corporation (JST) and JSPS KAKENHI Grants No. JP25107005, JP16K13845, JP26247064.

Appendix. Calculation of the eigen energies of the multi-orbital Hamiltonian for silane, germane and stannane

The basis of the Hamiltonian \mathcal{H}_{mol} is given by

$$\Psi^\dagger = (\psi_s, \psi_{p_x}, \psi_{p_y}, \psi_{p_z}, \phi_0, \phi_1, \phi_2, \phi_3) \quad (19)$$

where ψ_s , ψ_{p_x} , ψ_{p_y} and ψ_{p_z} are the bases of the s , p_x , p_y and p_z orbitals of the center atom. ϕ_0, ϕ_1, ϕ_2 and ϕ_3 are $1s$ orbitals of the four hydrogen atoms bonding the center atom. The corresponding Hamiltonian \mathcal{H}_{mol} is expressed by an 8×8 matrix:

$$\mathcal{H}_{mol} = \begin{pmatrix} \epsilon_s & 0 & 0 & 0 & V_{ss\sigma} & V_{ss\sigma} & V_{ss\sigma} & V_{ss\sigma} \\ 0 & \epsilon_p & 0 & 0 & V & V & -V & -V \\ 0 & 0 & \epsilon_p & 0 & V & -V & V & -V \\ 0 & 0 & 0 & \epsilon_p & V & -V & -V & V \\ V_{ss\sigma} & V & V & V & \epsilon_H & 0 & 0 & 0 \\ V_{ss\sigma} & V & -V & -V & 0 & \epsilon_H & 0 & 0 \\ V_{ss\sigma} & -V & V & -V & 0 & 0 & \epsilon_H & 0 \\ V_{ss\sigma} & -V & -V & V & 0 & 0 & 0 & \epsilon_H \end{pmatrix}, \quad (20)$$

with $V = \frac{V_{sp\sigma}}{\sqrt{3}}$. ϵ_s and ϵ_p are the on-site energies of the outer shell s orbital and the p orbital of the center atom, ϵ_H is the on-site energy of a hydrogen atom. We solve

$\mathcal{H}_{mol}\psi = E\psi$ and obtain eight eigen values analytically.

After unitary transformation using the following unitary matrix,

$$U = U_a U_b, \quad (21)$$

$$U_a = \begin{pmatrix} A & 0 \\ 0 & A \end{pmatrix}, \quad (22)$$

$$A = \begin{pmatrix} 1 & 0 & 0 & 0 \\ 0 & \frac{1}{\sqrt{3}} & \frac{1}{\sqrt{2}} & \frac{1}{\sqrt{6}} \\ 0 & \frac{1}{\sqrt{3}} & -\frac{1}{\sqrt{2}} & \frac{1}{\sqrt{6}} \\ 0 & \frac{1}{\sqrt{3}} & 0 & -\frac{2}{\sqrt{6}} \end{pmatrix}, \quad (23)$$

$$U_b = \begin{pmatrix} I & & 0 \\ & I & \\ & & B \\ 0 & & & I \end{pmatrix}, \quad (24)$$

$$I = \begin{pmatrix} 1 & 0 \\ 0 & 1 \end{pmatrix}, \quad (25)$$

$$B = \begin{pmatrix} \frac{1}{2} & \frac{\sqrt{3}}{2} \\ \frac{\sqrt{3}}{2} & -\frac{1}{2} \end{pmatrix}, \quad (26)$$

we change the basis as follows:

$$\begin{aligned} & U^\dagger \mathcal{H}_{mol} U \\ &= \begin{pmatrix} \epsilon_s & 0 & 0 & 0 & 2V_{ss\sigma} & 0 & 0 & 0 \\ 0 & \epsilon_p & 0 & 0 & 0 & 2V & 0 & 0 \\ 0 & 0 & \epsilon_p & 0 & 0 & 0 & 2V & 0 \\ 0 & 0 & 0 & \epsilon_p & 0 & 0 & 0 & 2V \\ 2V_{ss\sigma} & 0 & 0 & 0 & \epsilon_H & 0 & 0 & 0 \\ 0 & 2V & 0 & 0 & 0 & \epsilon_H & 0 & 0 \\ 0 & 0 & 2V & 0 & 0 & 0 & \epsilon_H & 0 \\ 0 & 0 & 0 & 2V & 0 & 0 & 0 & \epsilon_H \end{pmatrix}. \end{aligned} \quad (27)$$

We can transform the basis of equation (27) as follows:

$$\begin{aligned} & \begin{pmatrix} \epsilon_s & 2V_{ss\sigma} \\ 2V_{ss\sigma} & \epsilon_H \end{pmatrix} \oplus \begin{pmatrix} \epsilon_p & 2V \\ 2V & \epsilon_H \end{pmatrix} \oplus \begin{pmatrix} \epsilon_p & 2V \\ 2V & \epsilon_H \end{pmatrix} \\ & \oplus \begin{pmatrix} \epsilon_p & 2V \\ 2V & \epsilon_H \end{pmatrix}. \end{aligned} \quad (28)$$

Consequently, we can obtain the energy levels for silane, germane and stannane analytically.

Reference

- [1] Takeda K and Shiraishi K 1994 *Phys. Rev. B* **50** 14916
- [2] Cahangirov S, Topsakal M, Aktürk E, Şahin H and Ciraci S 2009 *Phys. Rev. Lett.* **102** 236804
- [3] Matthes L, Pulci O and Bechstedt F 2013 *J. Phys.: Condens. Matter* **25** 395305
- [4] Ezawa M *J. Phys. Soc. Jpn.* **84** 121003
- [5] Liu C C, Feng W and Yao Y 2011 *Phys. Rev. Lett.* **107** 076802
- [6] Drummond N D, Zólyomi V and Fal'ko V I 2012 *Phys. Rev. B* **85** 075423
- [7] Ezawa M 2012 *New J. Phys.* **14** 033003
- [8] Ezawa M 2012 *Phys. Rev. Lett.* **109** 055502
- [9] Xu Y, Yan B, Zhang H J, Wang J, Xu G, Tang P, Duan W and Zhang S C 2013 *Phys. Rev. Lett.* **111** 136804
- [10] Lalmi B, Oughaddou H, Enriquez H, Kara A, Vizzini S, Ealet B and Aufray B 2010 *Appl. Phys. Lett.* **97** 223109
- [11] Lin C L, Arafune R, Kawahara K, Tsukahara N, Minamitani E, Kim Y, Takagi N and Kawai M 2012 *Appl. Phys. Express* **5** 045802
- [12] Vogt P, De Padova P, Quaresima C, Avila J, Frantzeskakis E, Asensio M C, Resta A, Ealet B and Le Lay G 2012 *Phys. Rev. Lett.* **108** 155501
- [13] Feng B, Ding Z, Meng S, Yao Y, He X, Cheng P, Chen L and Wu K 2012 *Nano Lett.* **12** 3507–3511
- [14] Jamgotchian H, Colignon Y, Hamzaoui N, Ealet B, Hoarau J Y, Aufray B and Bibérian J P 2012 *J. Phys.: Condens. Matter* **24** 172001
- [15] Tao L, Cinquanta E, Chiappe D, Grazianetti C, Fanciulli M, Dubey M, Molle A and Akinwande D 2015 *Nat. Nanotechnol.* **10** 227–231
- [16] Fleurence A, Friedlein R, Ozaki T, Kawai H, Wang Y and Yamada-Takamura Y 2012 *Phys. Rev. Lett.* **108** 245501
- [17] Meng L, Wang Y, Zhang L, Du S, Wu R, Li L, Zhang Y, Li G, Zhou H, Hofer W A and Gao H J 2013 *Nano Lett.* **13** 685–690
- [18] Hoffmann R 2013 *Angew. Chem. Int. Ed.* **52** 93–103
- [19] Dávila M E, Xian L, Cahangirov S, Rubio A and Lay G L 2014 *New J. Phys.* **16** 095002
- [20] Li L, Lu S z, Pan J, Qin Z, Wang Y q, Wang Y, Cao G y, Du S and Gao H J 2014 *Adv. Mater.* **26** 4820–4824
- [21] Zhu F f, Chen W j, Xu Y, Gao C l, Guan D d, Liu C h, Qian D, Zhang S C and Jia J f 2015 *Nat. Mater.* **14** 1020–1025
- [22] Fujita M, Wakabayashi K, Nakada K and Kusakabe K 1996 *J. Phys. Soc. Jpn.* **65** 1920–1923
- [23] Okada S and Oshiyama A 2001 *Phys. Rev. Lett.* **87** 146803
- [24] Klein D J 1994 *Chem. Phys. Lett.* **217** 261 – 265
- [25] Klein* D J and Bytautas† L 1999 *J. Phys. Chem. A* **103** 5196–5210
- [26] Ryu S and Hatsugai Y 2002 *Phys. Rev. Lett.* **89** 077002
- [27] Hatsugai Y 2009 *Solid State Commun.* **149** 1061 – 1067
- [28] Kobayashi Y, Fukui K i, Enoki T, Kusakabe K and Kaburagi Y 2005 *Phys. Rev. B* **71** 193406
- [29] Zhang X, Yazyev O V, Feng J, Xie L, Tao C, Chen Y C, Jiao L, Pedramrazi Z, Zettl A, Louie S G, Dai H and Crommie M F 2013 *ACS Nano* **7** 198–202
- [30] Talirz L, Söde H, Cai J, Ruffieux P, Blankenburg S, Jafaar R, Berger R, Feng X, Müllen K, Passerone D, Fasel R and Pignedoli C A 2013 *J. Am. Chem. Soc.* **135** 2060–2063
- [31] Barone V, Hod O and Scuseria G E 2006 *Nano Lett.* **6** 2748–2754
- [32] Okada S 2008 *Phys. Rev. B* **77** 041408
- [33] Kunstmann J, Özdoğan C, Quandt A and Fehske H 2011 *Phys. Rev. B* **83** 045414
- [34] Yamanaka A and Okada S 2016 *Carbon* **96** 351 – 361
- [35] Kusakabe K and Maruyama M 2003 *Phys. Rev. B* **67** 092406
- [36] Ziatdinov M, Fujii S, Kusakabe K, Kiguchi M, Mori T and Enoki T 2013 *Phys. Rev. B* **87** 115427
- [37] Song Y L, Zhang Y, Zhang J M and Lu D B 2010 *Appl. Surf. Sci.* **256** 6313 – 6317

- [38] Seixas L, Padilha J E and Fazzio A 2014 *Phys. Rev. B* **89** 195403
- [39] Pang Q, Zhang Y, Zhang J M, Ji V and Xu K W 2011 *Nanoscale* **3** 4330–4338
- [40] Xu Y, Tang P and Zhang S C 2015 *Phys. Rev. B* **92** 081112
- [41] Fang Y, Huang Z Q, Hsu C H, Li X, Xu Y, Zhou Y, Wu S, Chuang F C and Zhu Z Z 2015 *Sci. Rep.* **5**
- [42] Liu C C, Jiang H and Yao Y 2011 *Phys. Rev. B* **84** 195430
- [43] Matthes L and Bechstedt F 2014 *Phys. Rev. B* **90** 165431
- [44] Slater J C and Koster G F 1954 *Phys. Rev.* **94** 1498–1524
- [45] Saito R, Fujita M, Dresselhaus G and Dresselhaus M S 1992 *Phys. Rev. B* **46** 1804–1811
- [46] Froyen S and Harrison W A 1979 *Phys. Rev. B* **20**(6) 2420–2422
- [47] Pedersen T G, Fisker C and Jensen V 2010 *J. Phys. Chem. Solids* **71** 18 – 23
- [48] Yao Y, Ye F, Qi X L, Zhang S C and Fang Z 2007 *Phys. Rev. B* **75** 041401
- [49] Chadi D J 1977 *Phys. Rev. B* **16** 790–796
- [50] Tanaya S 2014 *Numerical studies of edge states in hydrogen terminated silicene ribbons* Ph.D. thesis University of Tsukuba
- [51] Harrison W A 1989 *Electronic Structure and the Properties of Solids: The Physics of the Chemical Bond* (Dover)
- [52] Kane C L and Mele E J 2005 *Phys. Rev. Lett.* **95** 146802
- [53] The first-principles calculations were performed by the VASP (Vienna ab-initio simulation package) code [57, 58], which is based on the density functional theory (DFT) with the Perdew-Burke-Enzerhof generalized gradient approximation [59]. The core-valence interactions were described by projected-augmented-wave potentials [60].
- [54] Xiong W, Xia C, Peng Y, Du J, Wang T, Zhang J and Jia Y 2016 *Phys. Chem. Chem. Phys.* **18** 6534–6540
- [55] Ding Y and Ni J 2009 *Appl. Phys. Lett.* **95** 083115
- [56] Fang D Q, Zhang S L and Xu H 2013 *RSC Adv.* **3** 24075–24080
- [57] Kresse G and Furthmüller J 1996 *Phys. Rev. B* **54** 11169–11186
- [58] Kresse G and Joubert D 1999 *Phys. Rev. B* **59** 1758–1775
- [59] Perdew J P, Burke K and Ernzerhof M 1996 *Phys. Rev. Lett.* **77** 3865–3868
- [60] Blöchl P E 1994 *Phys. Rev. B* **50**(24) 17953–17979